Environmental Pollution 343 (2024) 123148

Contents lists available at ScienceDirect

Environmental Pollution

journal homepage: www.elsevier.com/locate/envpol

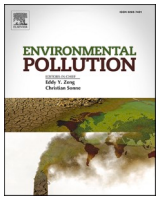

Biochar supported nanoscale zerovalent iron-calcium alginate composite for simultaneous removal of Mn(II) and Cr(VI) from wastewater: Sorption performance and mechanisms☆

Bing Wang [a,b,*], Chenxi Zhao [c], Qianwei Feng [a], Xinqing Lee [c], Xueyang Zhang [d], Shengsen Wang [e], Miao Chen [a]

[a] College of Resources and Environmental Engineering, Guizhou University, Guiyang, Guizhou, 550025, China
[b] Key Laboratory of Karst Georesources and Environment, Ministry of Education, Guizhou University, Guiyang, Guizhou, 550025, China
[c] State Key Laboratory of Environmental Geochemistry, Institute of Geochemistry, Chinese Academy of Sciences, Guiyang, Guizhou, 550081, China
[d] School of Environmental Engineering, Jiangsu Key Laboratory of Industrial Pollution Control and Resource Reuse, Xuzhou University of Technology, Xuzhou, Jiangsu, 221018, China
[e] College of Environmental Science and Engineering, Yangzhou University, Yangzhou, Jiangsu, 225127, China

ARTICLE INFO

Keywords:
Biochar
nZVI
Calcium alginate
Cr(VI)
Mn(II)
Site energy distribution analysis

ABSTRACT

Heavy metal pollution in water caused by industrial activities has become a global environmental issue. Among them, manganese mining and smelting activities have caused the combined pollution of Cr(VI) and Mn(II) in water, posing a serious ecotoxicological risk to ecological environments and human health. To efficiently remove Cr(VI) and Mn(II) from wastewater, a novel biochar supported nanoscale zerovalent iron-calcium alginate composite (CA/nZVI/RSBC) was synthesized by liquid-phase reduction and calcium alginate embedding methods. The adsorption performance and mechanisms of Cr(VI) and Mn(II) by CA/nZVI/RSBC were investigated. The maximum adsorption capacities of Cr(VI) and Mn(II) onto CA/nZVI/RSBC fitted by the Langmuir model were 5.38 and 39.78 mg/g, respectively, which were much higher than the pristine biochar. The iron release from CA/nZVI/RSBC was comparatively lower than that of nZVI/RSBC. Mn(II) presence enhanced the reduction of Cr(VI) by CA/nZVI/RSBC. The results of XRD, XPS, and site energy distribution analysis indicated that redox was the predominant mechanism of Cr(VI) adsorption, while electrostatic attraction dominated Mn(II) adsorption. This study provides a novel alternative way for the simultaneous removal of Cr(VI) and Mn(II) in wastewater.

1. Introduction

Water contamination has acquired prominence as a critical concern worldwide (Seliem et al., 2020). Natural water polluted by heavy metals can lead to disturbed ecosystems and threaten human health. Among them, the presence of Mn(II) and Cr(VI) in water is mainly attributed to metal smelting, leather and pigment manufacture, glass and ceramic industries, and mine mining (El-Korashy et al., 2016; Khan et al., 2020). In the environment, Cr is found mainly in hexavalent (Cr(VI)) and trivalent (Cr(III)) forms. Cr(VI) is much more hazardous than Cr(III), leading to serious medical disorders (such as human organ failure, chromosomal aberrations, and carcinogenesis) after enrichment through the food chain (Xu et al., 2021; Yüksel et al., 2021a). Meanwhile, excessive intake of Mn(II) can also cause problems in the central nervous system, liver, and lungs (Seliem et al., 2020). Therefore, exposure to heavy metals such as Cr(VI) and Mn(II) may cause an ecotoxicological risk (Topaldemir et al., 2023; Yüksel et al., 2021b). There is an urgent need for efficient treatment of Cr(VI) and Mn(II) composite polluted water. However, to date, limited research has been conducted on mitigating Cr(VI) and Mn(II) compound pollution simultaneously. Therefore, a technology to simultaneously effectively remove Mn(II) and Cr(VI) in wastewater is of great significance for the ecological environment, food safety, and human health.

Heavy metals are treated in wastewater mainly through physical,

☆ This paper has been recommended for acceptance by Dr Amit Bhatnagar.

* Corresponding author. College of Resources and Environmental Engineering, Guizhou University, Guiyang, Guizhou, 550025, China.
E-mail address: bwang6@gzu.edu.cn (B. Wang).

https://doi.org/10.1016/j.envpol.2023.123148
Received 15 October 2023; Received in revised form 6 December 2023; Accepted 11 December 2023
Available online 15 December 2023

chemical, and biological routes (Zhao et al., 2021b). Adsorption is one of the chemical remediation methods (Zhao et al., 2023a). The added adsorbents can decrease the contents of heavy metals in wastewater through precipitation, complexation, ion exchange, and redox reactions (Zhao et al., 2020b; Ziarati et al., 2023). Recently, biochar has gained significant attention as an efficient adsorbent due to its substantial specific surface area (SSA), rich functional groups (FGs), and complicated pore structures (Feng et al., 2022a). Through surface complexation, ion exchange, and the electrostatic effects mediated by negative charges on the biochar surface, biochar can attenuate the diffusion of metals in the environment and impede the migration of toxic substances (Feng et al., 2021b). Nonetheless, pristine biochar still exhibits a relatively constrained capacity for adsorbing pollutants compared with activated carbon. Therefore, a large number of studies have been directed at modifying biochar to enhance its adsorption capacity (Wang et al., 2017a; Zhao et al., 2022c).

Nanomaterials are widely used in various fields in terms of environment, agriculture, and medicine due to their unique and excellent physicochemical properties (Gunashova et al., 2021; Liu et al., 2023; Nasibova, 2023; Zhao et al., 2023a). Previously, there have been a lot of reports on the modification of biochar with nanomaterials or metal nano oxides (Zhao et al., 2021). Among them, nano-zero valent iron (nZVI) has notable attributes such as low cost, high SSA, high reducibility, high reactivity, and nano-sized particle feature (Zhao et al., 2023a). Thus an increasing number of studies are using nZVI modified biochar to remediate both heavy metals and organic pollutants in the environment (Ahmad et al., 2018; Han et al., 2023; Zhang et al., 2023a). Meanwhile, immobilizing nZVI onto a carbonaceous carrier is also beneficial for mitigating the agglomeration and reducing reactivity resulting from the high surface energy and strong magnetic force of nZVI (Wang et al., 2017b). However, it still faces some challenges during practical application. For example, nZVI is easily oxidized in the air, and may cause secondary pollution, producing toxic effects on organisms. So it is necessary to find a carrier to immobilize nZVI modified biochar.

Sodium alginate, a natural polysaccharide polymer, comprises negatively charged carboxyl groups that enable the electrostatic adsorption of cations while simultaneously facilitating chelation (Feng et al., 2022a; Wang et al., 2018a; Wang et al., 2019c). It can form calcium alginate (CA) hydrogel after cross-linking with Ca(II). As a porous, green, and environmentally friendly material, CA can be used to immobilize functional materials to advance their mechanical strength (Wang et al., 2018b). CA hydrogels are insoluble in water and can be used to capture toxic heavy metals (Mousa et al., 2016; Wang et al., 2019a). Nanoparticles embedded by CA not only have good mechanical strength and stability (Wang et al., 2018b), but also exhibit good adsorption effects on organic and inorganic pollutants (Bahrami et al., 2020; Zhao et al., 2023a). For example, Bahrami et al. (2020) synthesized CA microspheres impregnated with nZVI, magnetite nanoparticles, and activated carbon for the remediation of nitrate-contaminated groundwater. The results demonstrated the CA microspheres achieved a removal rate of 48.0%–65.0% for nitrate (100 mg/L) in wastewater within 48 h. Javadian et al. (2020) prepared CA-embedded carboxymethyl chitosan magnetic bio-nanocomposites and used them to adsorb rare earth elements, and found that under the optimal conditions (pH 5.5 and reaction time 40 min), the highest adsorption capacity fitted using Langmuir model of Nd^{3+} onto the composites was 73.37 mg/g. Our previous research also found that CA-embedded ball-milled biochar composites have good adsorption effects on heavy metals (Wang et al., 2018a; Zhao et al., 2023a), nutrients (Feng et al., 2022b; Wang et al., 2018c), SO_4^{2-}, and Fe^{3+} (Li et al., 2023) in water. However, current studies on CA-embedded biochar composites mainly focus on a single heavy metal in water, and lack of adsorption studies on multiple heavy metals (Abdelwahab et al., 2022). Especially, the effects and mechanisms of CA/nZVI/BC on the simultaneous removal of Cr(VI) and Mn(II) from water are still unknown. Using CA/nZVI/BC composites to adsorb Cr(VI) and Mn(II) from polluted water holds considerable promise for the remediation of pollutants in mining areas.

Based on the above reasons, CA/nZVI/BC composites that dispersed nZVI and reduced iron (Fe) release into the environment were successfully prepared and used to adsorb Cr(VI) and Mn(II) in polluted water. This study aims to (1) analyze the influencing factors of Mn(II) and Cr (VI) adsorption onto CA/nZVI/BC; (2) investigate the adsorption performance and behavior of Mn(II) and Cr(VI) by CA/nZVI/BC through adsorption models; (3) explore the adsorption mechanisms of Mn(II) and Cr(VI) on CA/nZVI/BC by combining XRD, XPS, and site energy distribution analysis. This study offers an alternative approach for addressing the removal of Cr(VI) and Mn(II) compound pollution in wastewater.

2. Materials and methods

2.1. Reagents and materials

Rice straw used to prepare biochar was collected in the suburban Huaxi District, Guizhou Province, China. Reagents essential for the experiments included concentrated nitric acid, sodium alginate, anhydrous calcium chloride, concentrated sulfuric acid, 1,5-diphenylcarbohydrazide, and hydrochloric acid (AR, Sinopharm Chemical Reagent Co., Ltd.), phosphoric acid, sodium hydroxide (AR, Chuandong Chemical Reagent Co., Ltd.), absolute ethanol, 95% ethanol (AR, Tianjin Fuyu Fine Chemical Reagent Co., Ltd.), potassium dichromate, hydroxylamine hydrochloride, and manganese chloride tetrahydrate (AR, Tianjin Kermel Chemical Reagent Co., Ltd.).

2.2. Preparation of CA/nZVI/BC composite

The collected rice straw was pretreated according to the method of Zhao et al. (2022c). A tube carbonization furnace (SG-GL1200 K, Shanghai Institute of Optics and Precision Instruments, Chinese Academy of Sciences) was used to carbonize rice straw. A 2.5 °C/min heatzing rate was applied to the furnace to raise the temperature to 300, 450, and 600 °C in the presence of as N_2 gas flow (Zhao et al., 2023b). The prepared biochar was milled and sieved through a 200 mesh sieve, which was labeled as RSBC. CA/nZVI/BC composite was prepared according to the method of Zhao et al. (2023a).

For the production of nZVI/RSBC, 2.70 g of $FeCl_3.6H_2O$ was dissolved in 100 mL deionized (DI) water and 0.1 mol/L NaOH solution was adopted to adjust the solution pH. 5.04 g of RSBC was added to the three-necked flask, the prepared $FeCl_3$ solution was poured, and N_2 was aerated to exhaust air for 10 min. An electric stirrer was used to stir at 500 rpm for 1 h, then a syringe was used to add 0.04 mol/L $NaBH_4$ dropwise. The speed of the stirrer was adjusted to 1000 rpm and stirred for 30 min. An absolute ethanol wash was followed by vacuum filtration and washing of the reacted solid after 1 h of precipitation. Following three rounds of washing, the material was introduced into a vacuum oven and subjected to drying at 70 °C for a duration of 24 h. The obtained solid was named nZVI/RSBC.

Regarding the preparation of CA/nZVI/BC, 2.50 g of sodium alginate powder was introduced into 250 mL of DI water and thoroughly mixed by stirring to prepare a 1% (w/v) alginate suspension. Then the prepared nZVI/RSBC was weighed 1.0 g into the alginate suspension, stirred and mixed well, and then dropped into 0.1 mol/L 1.0 L $CaCl_2$ solution by a peristaltic pump at a speed of 12.0 mL/min to form black microspheres (Feng et al., 2022a). After overnight stabilization, the microspheres were rinsed with DI water three times to eliminate any excess surface $CaCl_2$ and then put into a vacuum oven to dry at 90 °C. The obtained microspheres were named CA/nZVI/RSBC. The sodium alginate solution mixed without biochar was prepared following the same procedure described above to obtain CA microspheres as a control.

2.3. Characterization of RSBC and CA/nZVI/RSBC

Scanning electron microscopy/energy dispersive X-ray spectrometer

(SEM-EDS) (QUANTA FEG 250, USA) was utilized to observe the surface morphologies and elemental composition of both RSBC and its composites at a working voltage of 25 kV (Yüksel et al., 2023). The chemical bonds in a molecule of RSBC and its composites were assessed by producing an infrared absorption spectrum by Fourier transform infrared spectrometer (FTIR) (Nicolet iS10, Thermo Fisher Nicolet). For both RSBC and the composites, the SSA was measured through SSA detectors (Jubo X1000, Beijing Bioelectronics Technology Co., Ltd.). The Zeta potentials of RSBC and its composites were assessed using a Malvern Zetasizer Nano ZSE (Malvern Instruments, UK) (Zhang et al., 2023b). X-ray photoelectron spectroscopy (XPS) (K-Alpha, Thermo Scientific) was adopted to evaluate the chemical state designations in CA/nZVI/RSBC (Yüksel et al., 2023), and the operating conditions of XPS were 1486.6 eV excitation source, 12 kV voltage, and 400 μm beam spot. X-ray diffractometer (XRD) (D8 advance, Bruker AXS) was utilized to examine the surface crystal composition of CA/nZVI/RSBC after adsorption of Cr(VI) and Mn(II) using Cu target radiation over a scan range of $2\theta = 10–80^{\circ}$ at a scanning speed of 10°/min (Luo et al., 2022).

2.4. Batch adsorption experiments

The experimental procedures for batch experiments refer to our previous researches (Li et al., 2023; Zhao et al., 2023a). In a 50 mL centrifuge tube, 0.10 g of RSBC and its composites with varying pyrolysis temperatures (300, 450, and 600 °C), was carefully weighed. Subsequently, a 40 mL solution of $MnCl_2{\cdot}4H_2O$ (containing 100 mg/L Mn (II)) was added to the tube. Based on the pyrolysis temperature selection experiments mentioned earlier, the RSBC and its composites prepared at the optimal pyrolysis temperature were chosen. RSBC prepared at the optimum pyrolysis temperature was further used to prepare nZVI/RSBC and CA/nZVI/RSBC with different loading ratios of nZVI. The effects of different loading ratios (the mass ratios of RSBC and nZVI were 0, 0.05, 0.1, 0.15, and 0.2 wt%, respectively) on Mn(II) adsorption were explored. Then the optimal loading ratios of CA/nZVI/RSBC were selected. According to the results of the above two experiments, the dosage selection experiment was carried out, and the dosages of CA/nZVI/RSBC were set to 0.25, 0.5, 1.0, 2.0, 5.0, and 10.0 g/L, respectively.

Under optimal conditions, the effects of solution pH and coexisting ions on the adsorption of Cr(VI) and Mn(II) on CA/nZVI/RSBC were studied. In addition, adsorption kinetics and adsorption isotherms of Cr (VI) and Mn(II) were also conducted. $K_2Cr_2O_7$ and $MnCl_2{\cdot}4H_2O$ were used to configure 50 mg/L Cr(VI) solution, 100 mg/L Mn(II) solution, and their mixed solution. A pH of 2.0, 4.0, 6.0, 8.0, and 10.0 was achieved by adding 0.1 mol/L HCl or NaOH to the solution. The effects of competing ions on the adsorption of Cr(VI) and Mn(II) were investigated using 0.001, 0.01, and 0.1 mol/L NaCl, Na_2CO_3, Na_2SO_4, $NaNO_3$, KCl, $MgCl_2$, and $CaCl_2$ solution, respectively. The adsorption kinetics experiment was conducted by measuring the concentrations of Cr(VI) and Mn (II) at 0.083, 0.5, 1, 2, 4, 8, 16, and 24 h, respectively. In the adsorption isotherm experiment, the initial concentrations of Cr(VI) were set to 20, 40, 60, 80, and 100 mg/L, while those of Mn(II) were 40, 80, 120, 160, and 200 mg/L, respectively.

These experiments were conducted under constant conditions of 25 °C with continuous shaking at a rate of 200 rpm for 24 h (except adsorption kinetics), and the resulting mixture was filtered. A Flame Atomic Absorption Spectrometer (TAS-990, Puxi, Beijing) was used to determine the concentration of Mn(II) in the filtrate. The concentration of Cr(VI) was determined using the diphenylcarbohydrazide chromogenic method, measuring the absorbance at a wavelength of 540 nm with a visible light spectrophotometer (7200, Unicosh, Shanghai).

2.5. Regeneration performance evaluation

The regeneration performance of CA/nZVI/RSBC was evaluated to explore its reusability for adsorbing Cr(VI) and Mn(II). In brief, in a 50 mL centrifuge tube, 0.20 g of CA/nZVI/RSBC and 40 mL of mixed solution containing 50 mg/L Cr(VI) and 100 mg/L Mn(II) was added. After the adsorption reached equilibrium, the contents of Cr(VI) and Mn (II) in the solution were determined. CA/nZVI/RSBC was collected and extracted with 40 mL of 0.1 M HCl and NaOH for Mn(II) and Cr(VI), respectively. After 24 h of extraction, the concentrations of Mn(II) and Cr(VI) in the solution were determined, the collected CA/nZVI/RSBC was rinsed with DI water and vacuum dried at 50 °C. The above procedures were repeated 6 times to explore the regeneration performance of CA/nZVI/RSBC.

3. Results and discussion

3.1. Characterization of CA/nZVI/RSBC

The SSAs and pore volumes of RSBC, nZVI/RSBC, and CA/nZVI/RSBC were measured. As shown in Table 1, the loading of nZVI increased the total pore volume and SSA of RSBC by 6.15 and 6.50 times, which could provide more adsorption sites. The single point average pore radius of the three adsorbents was less than 2 nm, and all belonged to microporous materials. It can be seen from the measured pH that RSBC was alkaline, pH decreased after loading nZVI, while electrical conductivity (EC) increased (Table 1). After the addition of CA, the pH dropped to weak acidity, and the EC greatly increased, while the cation exchange capacity (CEC) increased, probably attributed to the additional Ca^{2+} in the adsorbent (Zhao et al., 2022c). However, the anion exchange capacity (AEC) of CA/nZVI/RSBC was lower than that of nZVI/RSBC, which might be due to the CA containing many acidic substances (Lawrinenko et al., 2016).

The surface morphological features of the composites were observed by SEM as shown in Fig. 1. It was observed that the RSBC particles were evenly distributed, with occasional larger particles. Due to the high-temperature pyrolysis at 600 °C, excessive volatile gases were released from the RSBC surface, which expanded the pores, resulting in the partial pore destruction of rice straw. After loading nZVI, it was observed that the surface of nZVI/RSBC was full of fine particles. Meanwhile, the Fe content was higher than RSBC, which could prove that nZVI was successfully loaded on RSBC with uniform distribution, indicating that RSBC could prevent the aggregation of nZVI. This observation was similar to the findings of (Qian et al., 2017). CA/nZVI/RSBC was an irregular spherical material with an uneven surface. This was probably because of the nZVI particle protrusions on the surface of BC. According to the EDS analysis, the loading of nZVI and the addition of CA changed the elemental composition of the composites. After loading nZVI, the surface Fe content of RSBC increased, and the surface Fe content of nZVI/RSBC was 66.5 times that of RSBC, which also proved that nZVI was effectively loaded on RSBC. The Ca and Cl contents of CA/nZVI/RSBC increased, and the proportion of Fe was lower than that of nZVI/RSBC. At this time, the surface Fe content of CA/nZVI/RSBC was 43.7 times that of RSBC.

The functional group changes of RSBC, nZVI/RSBC, and CA/nZVI/RSBC are shown in Fig. 2. Six main peaks were observed, which were the stretching vibration peak representing –OH (3422–3441 cm^{-1}) (Zhao et al., 2020a), C═O (1591–1619 cm^{-1}), C–O (1030–1110 cm^{-1}), aromatic C–H (2921–2927 cm^{-1} and 700–885 cm^{-1}), and Fe–O (473–573 cm^{-1}) (Fan et al., 2019). Compared with RSBC, the number of FGs on its surface was enhanced after modification. The vibration peaks of FGs═ in nZVI/RSBC and CA/nZVI/RSBC indicated that the modification increased the surface content of –OH and C═O. With the addition of CA, the aromatic C–H and C–O vibration peaks became stronger on the adsorbent surface, indicating that the addition of CA increased the FGs content on the adsorbent surface. The findings were similar to those of Wan et al. (2019).

The Zeta potential of RSBC decreased when pH increased (Fig. S1), with a distinct decrease observed between pH 2.0 and 4.0. When pH > 10.0, the decrease became large again. The changing trend of nZVI/RSBC was similar to that of RSBC, and its Zeta potential was positive at

Table 1
Physicochemical properties of RSBC, nZVI/RSBC, and CA/nZVI/RSBC.

Adsorbents	BET SSA (m^2/g)	Total pore volume per point (cm^3/g)	Single point mean pore radius (nm)	BJH adsorption can be the most aperture (nm)	pH	EC (μS/cm)	CEC (cmol/kg)	AEC (mmol/g)
RSBC	19.53	0.0114	1.17	2.40	10.59	2586.67	50.96	2.04
nZVI/RSBC	126.95	0.0703	1.11	2.30	9.59	3486.67	42.08	2.83
CA/nZVI/RSBC	21.61	0.0106	0.98	2.19	6.81	9513.33	73.76	1.59

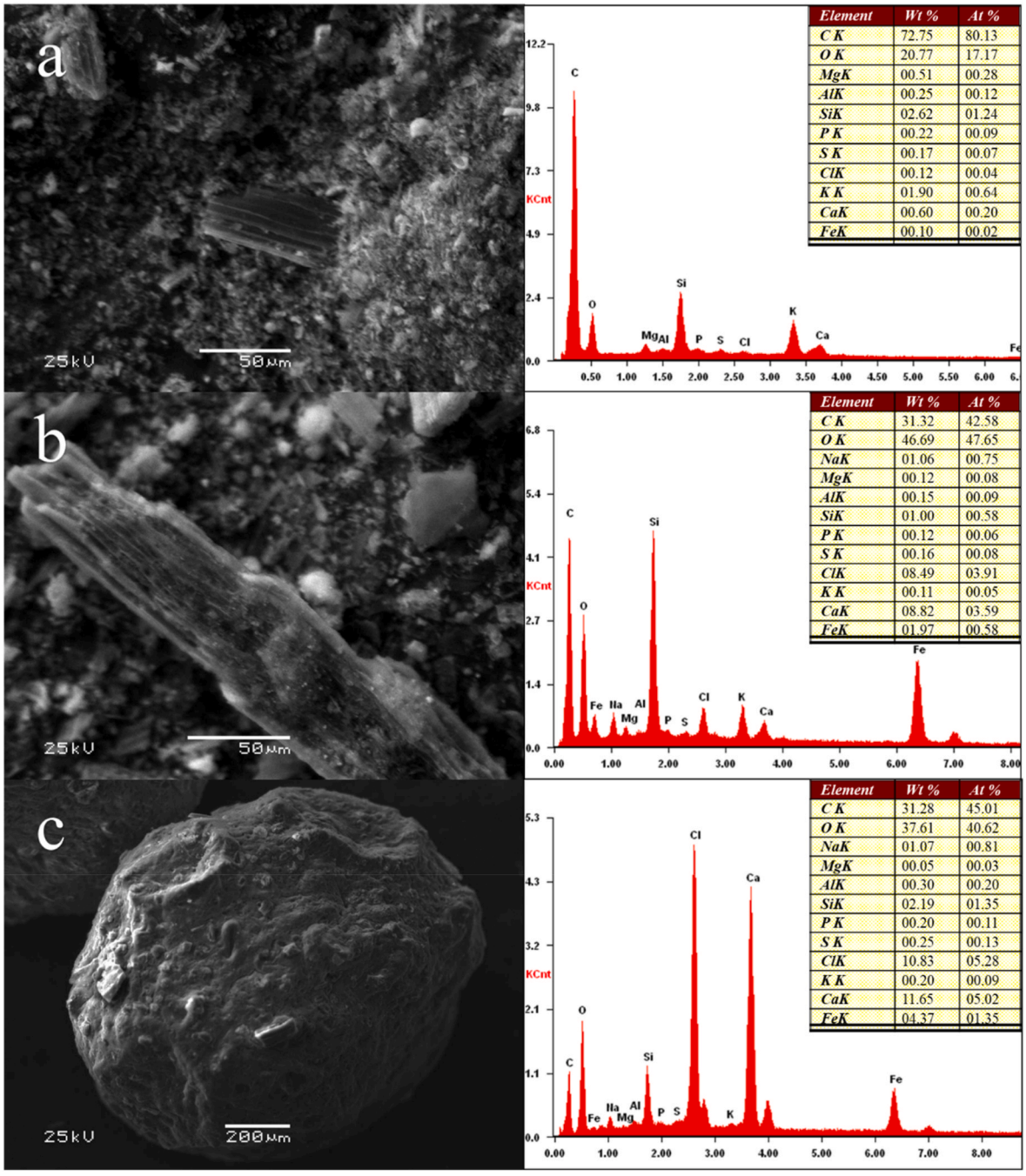

Fig. 1. SEM-EDS of RSBC (a), nZVI/RSBC (b), and CA/nZVI/RSBC (c).

pH 2.0. However, the Zeta potential of CA/nZVI/RSBC changed little with pH changing and remained negative within the pH range of 2.0–12.0. The surface of biochar was found to be positively charged when the solution pH was below the point of zero charge of CA/nZVI/RSBC. Conversely, the charge carried on the surface of biochar was negative (Zhao et al., 2021). Therefore, CA/nZVI/RSBC with consistently negative surface charge showed a better adsorption capacity on Mn(II).

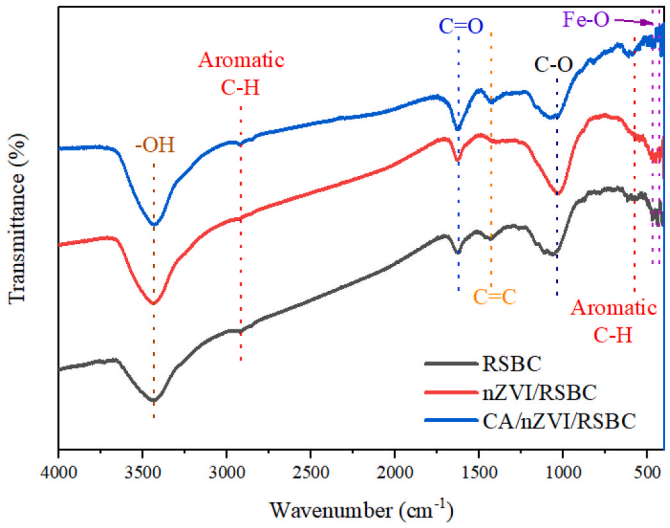

Fig. 2. FTIR spectra of RSBC, nZVI/RSBC, and CA/nZVI/RSBC.

3.2. Adsorption behaviors of Cr(VI) and Mn(II) by CA/nZVI/RSBC

3.2.1. Pyrolysis temperature

The influence of different influencing factors (solution pH, pyrolysis temperature of RSBC, loading ratio of nZVI, adsorbent dose, and coexisting ions) on the adsorptive removal of Cr(VI) and Mn(II) onto CA/nZVI/RSBC was investigated. Among them, the pyrolysis temperature, the loading ratios of nZVI, and the dosage were selected based on the influence on Mn(II). Fig. S2 shows the effect of RSBC, nZVI/RSBC, and CA/nZVI/RSBC on Mn(II) adsorption at various pyrolysis temperatures. The composites prepared from RSBC pyrolyzed at 600 °C showed the best adsorption capacities for Mn(II), probably due to the abundant pore structure of biochar pyrolyzed at elevated temperatures (Zhao et al., 2021). A study found that the contents of C, H, and N elements on the surface of biochar dropped with an increase in pyrolysis temperature (Aktar et al., 2022), the organic FGs onbiochar decreased, and the inorganic FG increased. As increasing pyrolysis temperature, the pH of biochar increased due to the strong alkalinity of biochar pyrolysis at high temperatures, which allowed cationic pollutants to be adsorbed (Gao et al., 2021). According to the study of Zhao et al. (2022b), the pH of sewage sludge biochar increased from 5.87 to 10.50 with the increase of pyrolysis temperatures (300, 500, and 700 °C). Also, the SSA of biochar increased from 5.26 m^2/g to 15.23 m^2/g. The pyrolysis enhanced the aromatization, stability, and decomposition of some oxygen-containing FGs of biochar. The elevated temperature facilitated the conversion of the bioavailable fraction to the more stable fraction, and the leaching rate of heavy metals was reduced by an average of 5.5%. This may be related to the decomposition of FGs, the collapse of pores, and the formation of new crystalline phases. As the pyrolysis temperature increased, the surface active sites of biochar experienced a reduction, while the SSA increased. Moreover, the amount of loaded 3-trimethoxysilylpropanethiol also increased. These changes contributed to an enhanced adsorption capacity for Hg(II) by facilitating surface adsorption, electrostatic interaction, ligand exchange, and surface complexation mechanisms.

3.2.2. Loading ratio of nZVI

RSBC, nZVI/RSBC, and CA/nZVI/RSBC produced at 600 °C were chosen for subsequent experiments. With increasing nZVI loading ratios of nZVI/RSBC and CA/nZVI/RSBC (Fig. S3a), the adsorption capacities for the Mn(II) increased but then declined, which was in agreement with the results of (Feng et al., 2021a). With nZVI loading ratios increased from 0 wt% to 0.1 wt%, nZVI particles were distributed on the surface of RSBC, providing more adsorption sites to react with pollutants. The adsorption capacities increased at the same time, indicating that nZVI played a role in the reaction. When the loading ratios of nZVI exceeded 0.1 wt%, excess nZVI particles might aggregate on the surface of RSBC. This blocked or even coated the active sites of RSBC, hindering electron transfer and resulting in a decline in the removal rate of Mn(II) (Dong et al., 2017; Yang et al., 2021a). According to Fig. S3 (b), the adsorption capacities of CA/nZVI/RSBC for Mn(II) increased first and then decreased with increasing nZVI loading ratios, reaching a maximum at nZVI loading ratio of 0.1 wt%, and higher than that of nZVI/RSBC, which could reach 17.91 mg/g for Mn(II). In the study of Yi et al. (2020), when the mass ratio between biochar and nZVI was 1:1, the elimination rate of Cr(VI) was 43.71%. When the mass ratio was 2:1, the elimination rate increased slowly, and then it was 100% after 2 h. A mass ratio of 3:1 led to 100% removal of Cr(VI) within 1 h. The more dispersed the nZVI, the more amount of active sites were, thereby increasing the contact opportunities of Cr(VI) with the active sites. The Fe release experiment showed that the Fe release of nZVI/RSBC was higher than that of CA/nZVI/RSBC when the nZVI loading ratio was more than 0.1 wt%, indicating that the addition of CA inhibited the release of Fe in the environment.

3.2.3. Adsorbent dosage

The removal rates of Mn(II) by RSBC, nZVI/RSBC, CA/nZVI/RSBC, and CA microspheres improved with an increase in dosage (Fig. S4). With 5.0 g/L of RSBC, nZVI/RSBC, CA/nZVI/RSBC, and CA microspheres, the removal rates of Mn(II) almost reached the maximum. The removal rates of Mn(II) were less improved by increasing the dosage. As the dosage increased, the active sites and FGs of RSBC, nZVI/RSBC, CA/nZVI/RSBC, and CA microspheres also increased, thus improving the removal rates of Mn(II) (Qiu et al., 2020). The adsorption sites of adsorbents could not satisfy the adsorption to Mn(II) in solution when the dosage was lower than 5 g/L, thus the Mn(II) removal rates were also relatively low. This result was similar to the findings of Lian et al. (2019). However, as the biochar dosage increased further, the removal rate of Cr(VI) enhanced slowly, and the authors finally selected 500 mg as the optimal dosage (Lian et al., 2019). Therefore, considering cost and pollutant removal rates, the optimal dosage of adsorbent was 5.0 g/L.

3.2.4. Solution pH

Adsorbent performance is greatly influenced by the pH of the solution. The figures depicted in Fig. 3 (a and b) illustrate the Cr(VI) adsorption patterns of RSBC, nZVI/RSBC, CA/nZVI/RSBC, and CA microspheres, while considering the presence of Mn(II). This phenomenon, referred to as Cr(VI) co-adsorption, was studied across a pH range of 2.0–10.0. RSBC, nZVI/RSBC, CA/nZVI/RSBC, and CA microspheres have decreased adsorption capacities to Cr(VI) as pH increases. Maximum adsorption capacities were observed at pH 2.0. A solution pH of 2.0 could allow Cr(VI) to adsorb on CA/nZVI/RSBC at a capacity of 22.67 mg/g. The observed variation in adsorption capacity can be attributed to the distinct forms of Cr(VI) in different solution pH conditions. At low pH, the primary species of Cr(VI) were $HCrO_4^-$ and $Cr_2O_7^{2-}$, which could be better adsorbed (Qian et al., 2017). Under acidic conditions, nZVI donated electrons to H^+, $HCrO_4^-$, and CrO_4^{2-} in solution, and reduced Cr(VI) to Cr(III), at which time Fe^0 was oxidized to Fe (II) or Fe(III) (Xu et al., 2021). A high pH condition, however, led to a negative charge on the adsorbent surface, which resulted in electrostatic repulsion between the adsorbent and Cr(VI), which prevented the reduction as well as adsorption of Cr(VI) (Fan et al., 2019). nZVI passivation could also be alleviated by low pH, and Cr(VI) could be effectively removed (Zhuang et al., 2021). Among them, the process of the redox reaction of Cr(VI) with nZVI/RSBC could be shown as the following equations (1)–(4) (Zhou et al., 2022):

$$3Fe^0 + 2HCrO_4^- + 14H^+ \rightarrow 3Fe^{2+} + 2Cr^{3+} + 8H_2O \quad (1)$$

$$3Fe^{2+} + HCrO_4^- + 7H^+ \rightarrow 3Fe^{3+} + Cr^{3+} + 4H_2O \quad (2)$$

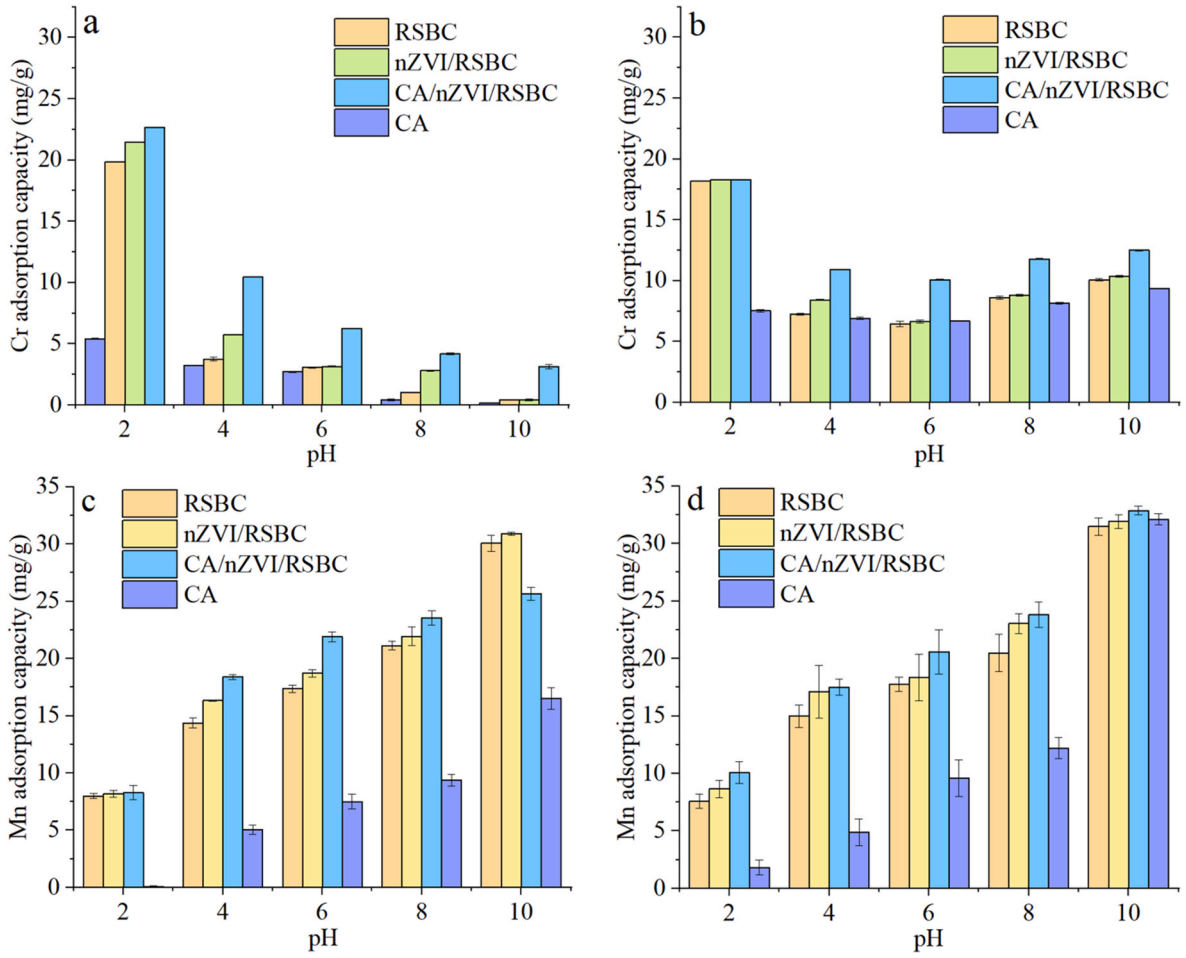

Fig. 3. Effect of solution pH on adsorption of Cr(VI) and Mn(II) by RSBC, nZVI/RSBC, and CA/nZVI/RSBC (a: Cr(VI); b: Cr(VI) co-adsorption; c: Mn(II); d: Mn(II) co-adsorption).

$$3Fe^0 + 2CrO_4^{2-} + 8H_2O \rightarrow 3Fe^{2+} + 2Cr^{3+} + 16OH^- \quad (3)$$

$$3Fe^{2+} + CrO_4^{2-} + 4H_2O \rightarrow 3Fe^{3+} + Cr^{3+} + 8OH^- \quad (4)$$

Adsorption of Mn(II) by RSBC, nZVI/RSBC, CA/nZVI/RSBC, and CA microspheres and the change in Mn(II) adsorption (hereafter referred to as Mn(II) co-adsorption) in the presence of Cr(VI) between pH 2.0–10.0 is presented in Fig. 3 (c and d). The adsorption capacities of Mn(II) by RSBC, nZVI/RSBC, CA/nZVI/RSBC, and CA microspheres increased with increasing solution pH. At low solution pH, the adsorption of Mn(II) was inhibited. This could be attributed to the abundance of H^+ in the solution, which competed with Mn(II) for the adsorption sites on the adsorbent surface (Yang et al., 2018). The H^+ concentration declined as the pH enhanced, and the competition between Mn(II) with H^+ for the adsorption sites decreased. However, precipitation was observed in Mn (II) solution when pH > 8.0, and the precipitation of Mn(II) was more obvious when pH was 10.0. At this time, a large amount of OH^- in the solution promoted Mn(II) conversion to $Mn(OH)_2$ precipitation. The pH of the solution was chosen to be 6.0 for subsequent experiments.

3.2.5. Coexisting ions

Fig. S5 (a and b) shows the influence of typical coexisting ions in water on nZVI/RSBC and CA/nZVI/RSBC on the adsorption of Cr(VI). Among them, the coexistence of Cl^- and NO_3^- both inhibited the adsorption of Cr(VI) by nZVI/RSBC and CA/nZVI/RSBC. The higher the concentration, the more obvious the inhibition effect. The existence of SO_4^{2-} in the solution accelerated the adsorption of Cr(VI), the higher the concentration, the more obvious the promotion effect. The coexistence of CO_3^{2-} promoted the adsorption of Cr(VI) on nZVI/RSBC, but inhibited the adsorption of Cr(VI) on CA/nZVI/RSBC. Cr(VI) removal by nZVI/RSBC and CA/nZVI/RSBC was minimally affected by solution cations. Cr (VI) adsorption by the adsorbents was not dominantly affected by elevated cations concentrations. Cations availability reduce Cr(VI) removal from the adsorbents due to their complexation with carboxyl groups in the adsorbents. Additionally, the complexation facilitated the attraction between nZVI particles, leading to accelerated aggregation and precipitation of nZVI, especially Ca^{2+} and Mg^{2+}. The coexistence of Na^+ had less effect, possibly due to the smaller redox potential of Na^+ compared to Cr(VI) (Xu et al., 2021). The effects of increasing cation concentration on the Cr(VI) adsorption capacities ranged from 75.46% to 94.5%, and the findings were consistent with (Sun et al., 2021).

The effects of commonly coexisting ions in wastewater on Mn(II) adsorption by nZVI/RSBC and CA/nZVI/RSBC are shown in Fig. S5 (c and d). The presence of cations in natural water inhibited the adsorption of Mn(II) by the adsorbents, and the effect was more obvious for ions with higher valence states. Possibly, the adsorption sites available on the adsorbent surface are more strongly bound to cations with higher valence states. When Na^+, K^+, Ca^{2+}, and Mg^{2+} ionic concentrations were 0.001 mol/L, the adsorption capacities of Mn(II) on CA/nZVI/RSBC were inhibited by 0, 10.68%, 19.47%, 15.85%, respectively. When the Na^+, K^+, Ca^{2+}, and Mg^{2+} concentrations were 0.01 mol/L, the adsorption capacities of Mn(II) on CA/nZVI/RSBC were inhibited by 3.93%, 17.59%, 33.91%, and 26.85%, respectively. When the Na^+, K^+, Ca^{2+}, and Mg^{2+} concentrations were 0.1 mol/L, the adsorption capacities of Mn(II) on CA/nZVI/RSBC were inhibited by 17.27%, 23.87%,

60.10%, and 52.56%, respectively. Except for CO_3^{2-}, the anions in the solution had minimal impact not detrimental effect on the removal of Mn(II) by nZVI/RSBC and CA/nZVI/RSBC, but the increase of anion concentration appeared to have a negative effect on the removal of Mn (II) by nZVI/RSBC and CA/nZVI/RSBC. Mn(II) disruption was slightly inhibited at 0.1 mol/L. The addition of CO_3^{2-} promoted the adsorption of Mn(II) on nZVI/RSBC and CA/nZVI/RSBC, probably because Mn(II) in solution first combined with CO_3^{2-} to form $MnCO_3$ precipitation, which promoted the adsorption of Mn(II). As the concentrations of CO_3^{2-} increased, the adsorption capacities of Mn(II) on CA/nZVI/RSBC were promoted by 2.97%, 8.10%, and 24.23%, respectively.

3.3. Adsorption kinetics

The changes of single and co-adsorption of Cr(VI) by RSBC, nZVI/RSBC, and CA/nZVI/RSBC over time are presented in Fig. S6 (a and b). The single adsorption leveled off after 2 h and the co-adsorption reached equilibrium after 1 h. At the onset of adsorption, the adsorption capacities of Cr(VI) on RSBC, nZVI/RSBC, and CA/nZVI/RSBC experienced a rapid surge, as Cr(VI) swiftly filled the adsorption sites on the CA/nZVI/RSBC surface. Subsequently, a gradual saturation of the adsorption sites on the surfaces of RSBC, nZVI/RSBC, and CA/nZVI/RSBC followed, and the increasing trend of Cr(VI) adsorption capacity ceased. The single adsorption and co-adsorption of Cr(VI) on CA/nZVI/RSBC were examined through an experiment, and the obtained data was fitted to the pseudo-first-order kinetic model (PFM) and pseudo-second-order kinetic model (PSM). Table S1 displays the fitting parameters. The PSM better fitted the adsorption process of Cr(VI) on CA/nZVI/RSBC (R^2 = 0.9819 and 0.9959), indicating that the adsorption processes of Cr(VI) on CA/nZVI/RSBC were predominantly driven by chemical adsorption (Teng et al., 2020).

The changes of single and co-adsorption of Mn(II) by RSBC, nZVI/RSBC, and CA/nZVI/RSBC over time are shown in Fig. S6 (c and d). The single adsorption of Mn(II) by RSBC, nZVI/RSBC, and CA/nZVI/RSBC reached equilibrium after 2 h, the co-adsorption leveled off after 1 h, and the changing trend was similar to that of Cr(VI). The kinetic experimental data of single adsorption and co-adsorption of Mn(II) by RSBC, nZVI/RSBC, and CA/nZVI/RSBC were fitted by using the PFM and PSM. Table S1 illustrates the fitting parameters. The PSM could better fit the adsorption process of CA/nZVI/RSBC on Mn(II) (R^2 = 0.9764 and 0.9918), indicating that the single adsorption and co-adsorption of CA/nZVI/RSBC onto Mn(II) were dominated by chemisorption (Teng et al., 2020).

3.4. Adsorption isotherms

Fig. 4 (a and b) illustrates the adsorption isotherms of Cr(VI) by RSBC, nZVI/RSBC, and CA/nZVI/RSBC at room temperature. Langmuir and Freundlich adsorption isotherm models were used to fit the experimental data. Among them, the Langmuir model is mainly used to describe homogeneous monolayer adsorption, there is no interaction between the adsorption molecules, and the adsorption process involves chemical and physical adsorption. The Freundlich model represents an empirical approach to describe the multi-layer chemical adsorption on heterogeneous surfaces (Zhang et al., 2022). As the initial concentration of Cr(VI) increased the adsorption of Cr(VI) by RSBC, nZVI/RSBC, and CA/nZVI/RSBC increased, but the increased range gradually decreased. At this time, the adsorbent surface had abundant adsorption sites, which could be fully contacted with Cr(VI), so that Cr(VI) could be easily adsorbed onto the adsorbents. Cr(VI) and adsorbents were able to fully

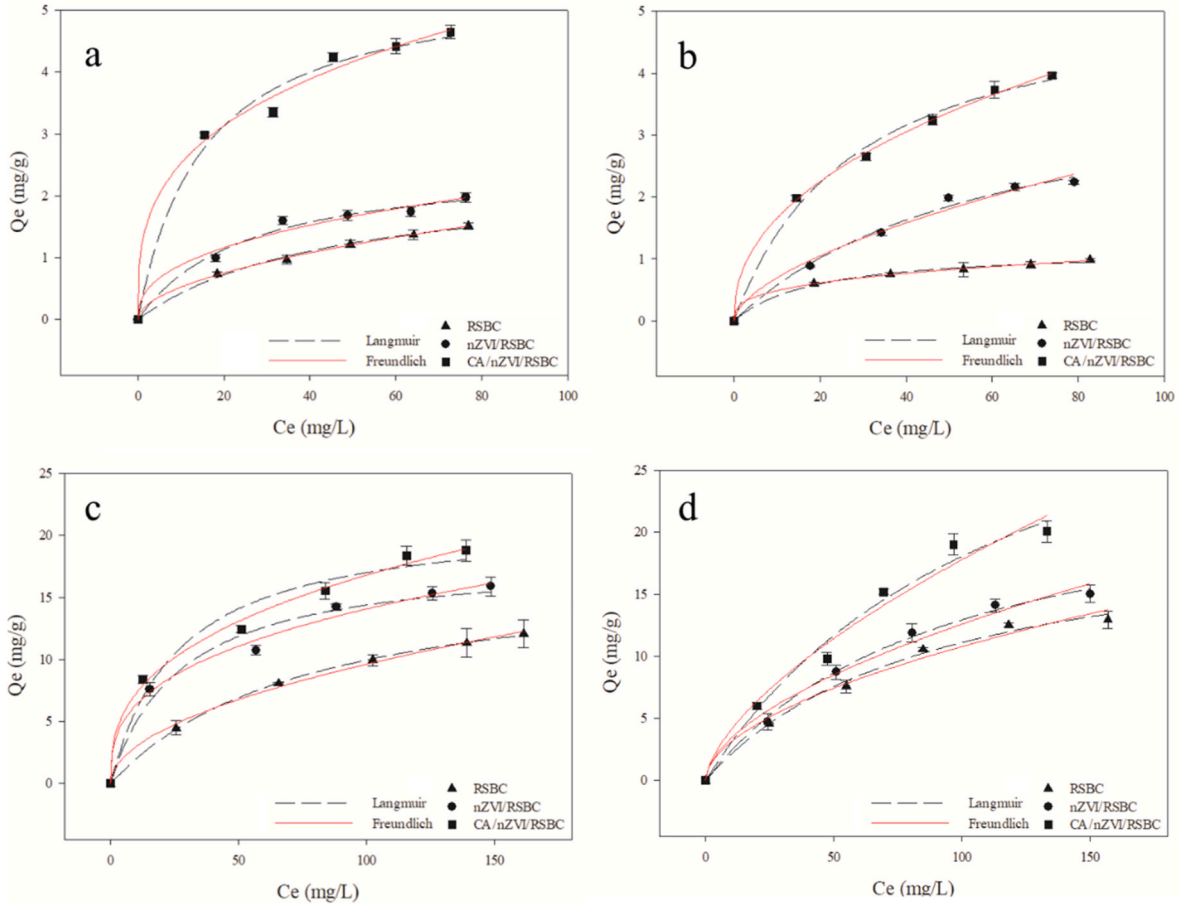

Fig. 4. Adsorption isotherms of Cr(VI) and Mn(II) on RSBC, nZVI/RSBC, and CA/nZVI/RSBC (a: Cr(VI); b: Cr(VI) co-adsorption; c: Mn(II); d: Mn(II) co-adsorption).

contact as Cr(VI) concentration increased, but the adsorption sites of the adsorbents gradually reached saturation, so adsorption capacities flattened out. Based on the regression coefficients R^2 in Table 2, both Langmuir and Freundlich models provided a good fit to the experimental data for RSBC, nZVI/RSBC, and CA/nZVI/RSBC adsorption of Cr(VI). The higher R^2 value of the Freundlich model suggested that the adsorption process occurred on the multi-molecular layer. CA/nZVI/RSBC exhibited a single adsorption maximum of 5.53 mg/g for Cr (VI) and a co-adsorption maximum of 5.38 mg/g by isotherm model fitting, which was higher than those of RSBC (2.36 and 1.17 mg/g) and nZVI/RSBC (2.58 and 4.14 mg/g), indicating that the presence of Mn(II) was favorable for Cr(VI) adsorption by CA/nZVI/RSBC.

Similarly, Fig. 4 (c and d) depicted the changes in Mn(II) adsorption capacities by RSBC, nZVI/RSBC, and CA/nZVI/RSBC at different initial Mn(II) concentrations. The adsorption capacities of Mn(II) by RSBC, nZVI/RSBC, and CA/nZVI/RSBC also increased, and the increasing trend was gradually flattened with the rise in the initial concentration of the solution. With increasing initial concentrations, the adsorbent became more in contact with Mn(II), but the adsorption sites on the adsorbent gradually became saturated. As indicated by R^2 (Table 2), both Langmuir and Freundlich models fit the experimental data well for Mn(II) adsorption by CA/nZVI/RSBC. In the case of Mn(II) single adsorption, the higher R^2 value of the Freundlich model suggested that the adsorption process took place on a polymolecular layer. However, for the co-adsorption of Mn(II), the Langmuir model was more accurate in predicting the adsorption process, demonstrating that the process occurred on the monomolecular layer. CA/nZVI/RSBC exhibited the maximum capacity of 21.49 mg/g for single adsorption and 39.78 mg/g for co-adsorption for Mn(II) by the isotherm model, which was higher than those of RSBC (17.79 and 21.01 mg/g) and nZVI/RSBC (18.28 and 25.19 mg/g). The 1/n value in the adsorption process was in the range of 0–1, reflecting that both Cr(VI) and Mn(II) were easily adsorbed by CA/nZVI/RSBC, and chemisorption was dominant (Wang et al., 2018d).

3.5. Adsorption thermodynamics

Different environmental temperatures affected the adsorption of Cr (VI) and Mn(II) by CA/nZVI/RSBC. Fig. S7 reflects the single adsorption and co-adsorption of Cr(VI) and Mn(II) by CA/nZVI/RSBC at reaction temperatures of 15, 25, and 35 °C as a function of the initial solution concentration. Fitting the experimental data using the Langmuir adsorption isotherm model was performed. The findings suggested that the adsorption capacities of both Cr(VI) and Mn(II) by CA/nZVI/RSBC increased as the initial concentrations of Cr(VI) and Mn(II) increased. However, the extent of this increase gradually diminished. This was assigned to the numerous adsorption sites on the adsorbent surface, which were able to make sufficient contact with Cr(VI) and Mn(II) at the lower initial solution concentration. With increasing reaction temperature, it was observed that the adsorption capacities of CA/nZVI/RSBC for Cr(VI) and Mn(II) reached their maximum at 35 °C. The possibility and extent of the adsorption reaction can be inferred by studying the thermodynamic parameters. Table S2 displays the thermodynamic parameters associated with the adsorption of pollutants by CA/nZVI/RSBC. At these temperatures, ΔG^0 valves were negative during the adsorption process of pollutants by each adsorbent, progressively decreased as the temperature increased, suggesting that both the single adsorption and co-adsorption of Cr(VI) and Mn(II) were feasible and spontaneous on CA/nZVI/RSBC. A more negative value indicated a more thorough reaction, and the adsorption capacities for Cr(VI) and Mn(II) improved with increasing temperature. ΔS^0 valves were all positive, indicating the good affinity of Cr(VI) and Mn(II) for CA/nZVI/RSBC and the spontaneous increase of liquid-solid-phase interactions on the surface of CA/nZVI/RSBC during the adsorption process. $\Delta H^0 > 0$, reflecting that the removal processes of Cr(VI) and Mn(II) by CA/nZVI/RSBC were mainly endothermic and chemical (Wang et al., 2019b).

3.6. Adsorption mechanisms

The morphological changes of CA/nZVI/RSBC before and after adsorption were detected. As shown in Fig. S8, before the adsorption of pollutants, the surface of CA/nZVI/RSBC was uneven, and large particles of nZVI/RSBC were observed on the surface. It was monitored that the surface of CA/nZVI/RSBC was covered by a layer of material with metallic luster after the adsorption of Cr(VI). Based on the SEM-EDS-mapping images (Fig. S9), it was evident that the distribution of Cr elements appeared on the surface of CA/nZVI/RSBC following the adsorption of Cr(VI), indicating the successful adsorption of Cr(VI). More particles were monitored on the surface of CA/nZVI/RSBC after the adsorption of Mn(II). After co-removal of Cr(VI) and Mn(II), the above two results were simultaneously observed on the CA/nZVI/RSBC surface. Combined with the SEM-EDS-mapping images of the CA/nZVI/RSBC surface, Mn(II) and Cr(VI) were simultaneously adsorbed.

As shown in Fig. S10, the compositional changes of the surface particles of CA/nZVI/RSBC before and after the adsorption of Cr(VI) and Mn(II) were analyzed by XRD patterns. It could be seen that the diffraction peaks of CA/nZVI/RSBC after the adsorption of pollutants were quite different from those before adsorption. For CA/nZVI/RSBC, diffraction peaks of FeOOH, Fe_2O_3, Fe_3O_4, and Fe^0 were observed at $2\theta = 21.1°$, 30.1°, 35.2°, and 44.7° (Yang et al., 2021a; Yi et al., 2020). This indicated that the nZVI in the adsorbent was oxidized. It was a typical nZVI core-shell structure, in which the peak at 44.7° was not obvious, which might be due to the increase of the molecular distance and the amorphous degree of the adsorbent by the addition of CA (Wan et al., 2019). After single adsorption of Mn(II) on CA/nZVI/RSBC, it was observed that the diffraction peaks of $C_{15}H_{21}MnO_6$, Mn_3O_4, $MnFe_2O_4$, and $MnCO_3$ increased at $2\theta = 15.8°$, 34.1°, 43.1°, and 60.1° (Yankovych et al., 2021). It showed that Mn(II) in solution reacted with Fe compounds in CA/nZVI/RSBC and formed $MnFe_2O_4$ species, and

Table 2
The adsorption isotherm fitting parameters of RSBC, nZVI/RSBC, and CA/nZVI/RSBC.

Adsorbents	Adsorbates	Langmuir			Freundlich		
		Q_m (mg/g)	k_L	R^2	k_F	1/n	R^2
RSBC	Cr(VI)	2.36	0.0220	0.9955	0.1587	0.5187	0.9988
nZVI/RSBC	(without Mn(II))	2.58	0.0391	0.9872	0.3534	0.3963	0.9799
CA/nZVI/RSBC		5.53	0.0654	0.9872	1.2320	0.3113	0.9924
RSBC	Cr(VI)	1.17	0.0524	0.9955	0.2297	0.3262	0.9993
nZVI/RSBC	(with Mn(II))	4.14	0.0162	0.9917	0.1769	0.5938	0.9839
CA/nZVI/RSBC		5.38	0.0355	0.9938	0.6035	0.4394	0.9990
RSBC	Mn(II)	17.79	0.0127	0.9996	0.9223	0.5089	0.9974
nZVI/RSBC	(without Cr(VI))	18.28	0.0370	0.9788	2.8666	0.3452	0.9927
CA/nZVI/RSBC		21.49	0.0379	0.9725	3.1427	0.3639	0.9952
RSBC	Mn(II)	21.01	0.0112	0.9937	0.8932	0.5407	0.9845
nZVI/RSBC	(with Cr(VI))	25.19	0.0105	0.9966	0.9157	0.5689	0.9857
CA/nZVI/RSBC		39.78	0.0083	0.9842	0.9420	0.6379	0.9771

ion-exchanged with CO_3^{2-} in adsorbent to form $MnCO_3$ precipitation (Yankovych et al., 2021). After single adsorption of Cr(VI) on CA/nZVI/RSBC, it was observed that the diffraction peaks of $C_{15}H_{21}MnO_6$ and $FeCr_2O_4$ were increased at $2\theta = 15.0°$ and 63.0°, which were attributed to the stable compound formed by Cr(III) and Fe(II) (Qiu et al., 2020). After CA/nZVI/RSBC co-adsorbed Mn(II) and Cr(VI), the diffraction peaks of the compounds contained in the above spectra were observed on the spectrum, indicating that the above reactions occurred during the co-adsorption process.

To better analyze the overlaid adsorption mechanisms of Cr(VI) and Mn(II), the XPS spectra of CA/nZVI/RSBC before and after the adsorption of Cr(VI) and Mn(II) were compared (Fig. S10). The C 1s, O 1s, and Fe 2p associated peaks were noticed at the positions of about 285.0 eV, 530.0 eV, and 710.0 eV from the XPS total spectrum of CA/nZVI/RSBC before the reaction. The Cr 2p peak was observed around 580 eV and the Mn 2p peak was observed around 630 eV after the reaction. Indicating that the Cr(VI) and Mn(II) were successfully adsorbed onto CA/nZVI/RSBC. The C 1s peaks can be assigned to C–C (284.5 eV), C–O (285.3 eV), and C═O (286.3 eV), respectively. The O 1s peaks correspond to C–O (532.1 eV), C═O (531.3 eV), and metal oxides (536.1 eV) (Yang et al., 2021a); Ca 2p peaks correspond to Ca–O (346.7 and 350.1 eV) and Ca–OH (350.8 eV), respectively. The areas of C–C and Ca–OH increased while those of C–O, C═O, and Ca–O peaks decreased after the Cr(VI) and Mn(II) were adsorbed, indicating that the above chemical bonds all participated in the reaction in the adsorption process, especially the oxygen-containing FGs. After Cr(VI) adsorption, the proportion of Fe(II) on the surface of CA/nZVI/RSBC decreased and the proportion of Fe(III) increased. It indicates that Fe participated in the redox reaction during the adsorption of Cr(VI), and Fe(II) was oxidized by Cr(VI) to produce more Fe(III) (Zhang et al., 2020). The proportion of Fe with different valence states on the surface of CA/nZVI/RSBC after Mn(II) adsorption was as follows: 55.98% Fe(II) and 44.02% Fe(III), which indicated that Fe and Mn conjugates on the adsorbent existed in the form of mixed-valence states after Mn(II) adsorption (Chen et al., 2020). The proportion of Fe with different valence states on the surface of CA/nZVI/RSBC after co-adsorption was: 45.51% Fe(II) and 54.49% Fe(III), indicating that Fe contributed in the redox reaction of Cr(VI) and Mn(II) at the same time. After Mn(II) was single adsorbed by CA/nZVI/RSBC, 92.89% of them participated in redox reactions and existed on the surface of CA/nZVI/RSBC in the form of Mn(III) as well as Mn(VI), while 84.08% of Mn(II) was oxidized after co-adsorption. Based on the findings from XRD analysis, Mn(II) was oxidized to Mn(VI) by redox reaction with Fe during the adsorption process, and combined with Fe to form $MnFeO_4$ precipitation. Following the single adsorption of Cr(VI) by CA/nZVI/RSBC, approximately 75.02% of Cr(VI) underwent reduction to Cr(III). In the case of co-adsorption, a slightly higher reduction of 75.72% was observed. These results suggest that the majority of Cr existed in the form of Cr(III). Moreover, negatively charged Cr(VI) was reduced to Cr(III) upon migrating to the surface of CA/nZVI/RSBC. Combined with the results of XRD analysis, Cr(III) joined with Fe(II) to form $FeCr_2O_4$ precipitates. Following co-adsorption, there was a reduction in the peak area of Mn(VI) and an increase in the peak areas of Fe(II) and Cr(III). This observation suggests that the simultaneous presence of Fe and Mn potentially enhances the reduction of Cr(VI). The presence of Mn(III) can be attributed to Cr(VI) reduction by $H_2C_2O_4$, –COOH, and –OH with Mn(II) oxidized to Mn(III) form (Huang et al., 2022).

Site energy distribution analysis was conducted to further examine the mechanisms involved in the adsorption of Mn(II) and Cr(VI) by CA/nZVI/RSBC. As shown in Fig. 5(a and b), the frequency distributions of adsorption site energy for Cr(VI) and Mn(II) by CA/nZVI/RSBC were all asymmetrical monomodal shapes, and the F (E*) value increased with increasing temperature, indicating that increasing temperature would raise the overall site energy distribution. The adsorption site energy distribution curve area simultaneously increased, so that more binding sites on CA/nZVI/RSBC were activated and thus the adsorption capacities of CA/nZVI/RSBC for Cr(VI) and Mn(II) were also improved (Yang et al., 2021b; Zhao et al., 2022a), which was in agreement with the experimental results. When E* = 20–30 kJ/mol, a significant number of chemical bonds existed between the surface of CA/nZVI/RSBC and Cr (VI) and Mn(II) (Cheng et al., 2021), a higher E* indicated more chemisorption participation as well as a more homogeneous adsorbent surface (Li et al., 2021). The adsorption sites of CA/nZVI/RSBC for Cr (VI) were concentrated at 18–26 kJ/mol, which indicated that the adsorption process was mainly through Cr(VI) binding with oxygen-containing FGs (-OH, –COOH, etc.) (Zhao et al., 2022b). CA/nZVI/RSBC bound to Fe^0 on the surface of CA/nZVI/RSBC through a weak electrostatic interaction with Cr(VI), and this result was consistent with the study carried out by (Liao et al., 2020). Then redox and complexation reactions took place between Cr(VI) and oxygen-containing FGs on the surface of CA/nZVI/RSBC. Electrostatic attraction was found to be the dominant factor in the adsorption of Mn(II) by CA/nZVI/RSBC, with chemical bonding playing a secondary role in the adsorption process for both pollutants. The primary adsorption mechanisms of Cr(VI) and Mn (II) on CA/nZVI/RSBC are illustrated in Fig. 6.

3.7. Stability and regeneration

Considering the economic effect of CA/nZVI/RSBC, its stability and reusability should also be considered when applied in practical

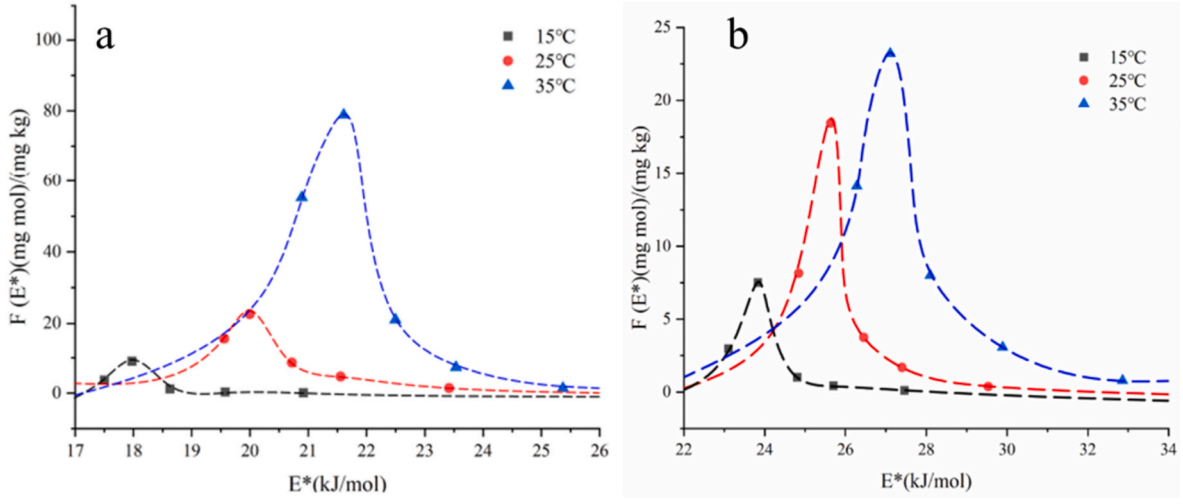

Fig. 5. Site energy distribution analysis of Cr(VI) (a) and Mn(II) (b) adsorption onto CA/nZVI/RSBC.

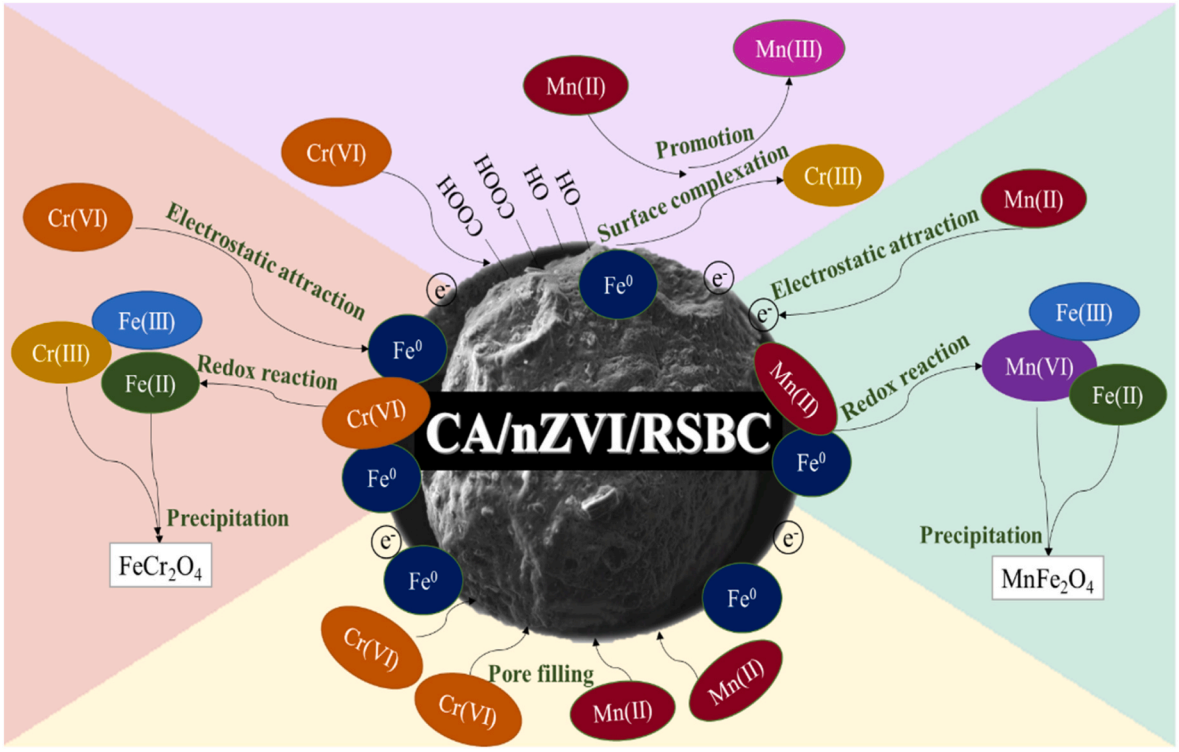

Fig. 6. The main adsorption mechanisms of Cr(VI) and Mn(II) by CA/nZVI/RSBC.

situations. As depicted in Fig. S11 (a), the adsorbed Cr(VI) on CA/nZVI/RSBC was desorbed using 0.1 mol/L NaOH, followed by six cycles of Cr (VI) adsorption. After the first adsorption-desorption, CA/nZVI/RSBC maintained a good adsorption capacity for Cr(VI). During the sixth adsorption cycle, CA/nZVI/RSBC exhibited the ability to adsorb 0.31 mg/g of Cr(VI), demonstrating its potential for reusability in the removal of Cr(VI) (Sahu et al., 2022). The decrease of adsorption capacity of CA/nZVI/RSBC by Cr(VI) could be attributed to the surface passivation caused by the formation of precipitated species on the surface of CA/nZVI/RSBC, and the continuously reduced active sites were also responsible for the decreased Cr(VI) adsorption by CA/nZVI/RSBC (Zhuang et al., 2021). This result was comparable to that of (Jia et al., 2021), and the removal rate of Cr(VI) by almond husk BC could still reach 48.5% after five desorption times. As shown in Fig. S11 (b), CA/nZVI/RSBC after adsorption of Mn(II) was desorbed by 0.1 mol/L HCl, and then Mn(II) was cyclically adsorbed for six cycles. After the third adsorption-desorption, CA/nZVI/RSBC maintained a good adsorption capacity (14.88 mg/g) for Mn(II). At the sixth adsorption, the Mn(II) adsorption of CA/nZVI/RSBC remained at 5.91 mg/g, which proved that CA/nZVI/RSBC was an excellent Mn(II) reusable adsorbent (Abd El et al., 2019).

Therefore, from the above results, it can be seen that CA/nZVI/RSBC has good application potential in simultaneously reducing Cr(VI) and Mn(II) from wastewater. This further indicates that CA/nZVI/RSBC can greatly reduce the risks that Cr(VI) and Mn(II) pose to the ecological environment.

4. Conclusions

In this research, nZVI/RSBC was synthesized using a liquid-phase reduction method and embedded with CA to obtain CA/nZVI/RSBC microspheres. The application of CA/nZVI/RSBC had demonstrated a favorable efficacy in the simultaneous removal of Cr(VI) and Mn(II). The iron release exhibited by the CA/nZVI/RSBC was comparatively lower in comparison to the iron release observed in the nZVI/RSBC. The inclusion of Mn(II) facilitated the reduction of Cr(VI) by the use of a composite consisting of CA, nZVI, and RSBC. The primary adsorption mechanism of Cr(VI) by CA/nZVI/RSBC was reduction, while these of Mn(II) was electrostatic attraction. In general, CA/nZVI/RSBC exhibits promising potential as an efficient and environmentally friendly composite for the concurrent removal of Cr(VI) and Mn(II) from polluted water.

CRediT authorship contribution statement

Bing Wang: Conceptualization, Formal analysis, Funding acquisition, Methodology, Writing - review & editing. **Chenxi Zhao:** Formal analysis, Methodology, Writing - original draft. **Qianwei Feng:** Writing - review & editing, Formal analysis. **Xinqing Lee:** Writing - review & editing. **Xueyang Zhang:** Formal analysis, Writing - review & editing. **Shengsen Wang:** Formal analysis, Writing - review & editing. **Miao Chen:** Writing – review & editing.

Declaration of competing interest

The authors declare that they have no known competing financial interests or personal relationships that could have appeared to influence the work reported in this paper.

Data availability

Data will be made available on request.

Acknowledgments

This work was supported by the National Natural Science Foundation of China (41977297), the Key Project of Science and Technology Department of Guizhou Province [ZK(2022)016], the Special Fund for Outstanding Youth Talents of Science and Technology of Guizhou Province [YQK[2023]014], the Special Research Fund of Natural Science (Special Post) of Guizhou University [(2020)01], and the Key Cultivation Program of Guizhou University [2019(08)].

Appendix A. Supplementary data

Supplementary data to this article can be found online at https://doi.org/10.1016/j.envpol.2023.123148.

References

Abd El, H., El Seleman, M.M., Saad, E.M., 2019. Applicability of water-spray electric arc furnace steel slag for removal of Cd and Mn ions from aqueous solutions and industrial wastewaters. J. Environ. Chem. Eng. 7 (2), 102915.

Abdelwahab, M.S., El Halfawy, N.M., El-Naggar, M.Y., 2022. Lead adsorption and antibacterial activity using modified magnetic biochar/sodium alginate nanocomposite. Int. J. Biol. Macromol. 206, 730–739.

Ahmad, M., Ahmad, M., Usman, A.R.A., Al-Faraj, A.S., Abduljabbar, A.S., Al-Wabel, M.I., 2018. Biochar composites with nano zerovalent iron and eggshell powder for nitrate removal from aqueous solution with coexisting chloride ions. Environ. Sci. Pollut. Control Ser. 25 (26), 25757–25771.

Aktar, S., Hossain, M.A., Rathnayake, N., Patel, S., Gasco, G., Mendez, A., Cicero, d.F., Surapaneni, A., Shah, K., Paz Ferreiro, J., 2022. Effects of temperature and carrier gas on physico-chemical properties of biochar derived from biosolids. J. Anal. Appl. Pyrol. 164, 105542.

Bahrami, F., Yu, X., Zou, Y., Sun, Y., Sun, G., 2020. Impregnated calcium-alginate beads as floating reactors for the remediation of nitrate-contaminated groundwater. Chem. Eng. J. 382, 122774.

Chen, L., Jiang, X., Xie, R., Zhang, Y., Jin, Y., Jiang, W., 2020. A novel porous biochar-supported Fe-Mn composite as a persulfate activator for the removal of acid red 88. Separ. Purif. Technol. 250, 117232.

Cheng, N., Wang, B., Feng, Q., Zhang, X., Chen, M., 2021. Co-adsorption performance and mechanism of nitrogen and phosphorus onto eupatorium adenophorum biochar in water. Bioresour. Technol. 340, 125696.

Dong, H., Deng, J., Xie, Y., Zhang, C., Jiang, Z., Cheng, Y., Hou, K., Zeng, G., 2017. Stabilization of nanoscale zero-valent iron (nZVI) with modified biochar for Cr(VI) removal from aqueous solution. J. Hazard Mater. 332, 79–86.

El-Korashy, S.A., Elwakeel, K.Z., El-Hafeiz, A.A., 2016. Fabrication of bentonite/thiourea-formaldehyde composite material for Pb(II), Mn(VII) and Cr(VI) sorption: a combined basic study and industrial application. J. Clean. Prod. 137, 40–50.

Fan, Z., Zhang, Q., Gao, B., Li, M., Liu, C., Qiu, Y., 2019. Removal of hexavalent chromium by biochar supported nZVI composite: batch and fixed-bed column evaluations, mechanisms, and secondary contamination prevention. Chemosphere 217, 85–94.

Feng, K., Xu, Z., Gao, B., Xu, X., Zhao, L., Qiu, H., Cao, X., 2021a. Mesoporous ball-milling iron-loaded biochar for enhanced sorption of reactive red: performance and mechanisms. Environ. Pollut. 290, 117992.

Feng, Q., Chen, M., Wu, P., Zhang, X., Wang, S., Yu, Z., Wang, B., 2022a. Calcium alginate-biochar composite as a novel amendment for the retention and slow-release of nutrients in karst soil. Soil Tillage Res. 223, 105495.

Feng, Q., Chen, M., Wu, P., Zhang, X., Wang, S., Yu, Z., Wang, B., 2022b. Simultaneous reclaiming phosphate and ammonium from aqueous solutions by calcium alginate-biochar composite: sorption performance and governing mechanisms. Chem. Eng. J. 429, 132166.

Feng, Q., Wang, B., Chen, M., Wu, P., Lee, X., Xing, Y., 2021b. Invasive plants as potential sustainable feedstocks for biochar production and multiple applications: a review. Resour. Conserv. Recycl. 164, 105204.

Gao, L., Li, Z., Yi, W., Li, Y., Zhang, P., Zhang, A., Wang, L., 2021. Impacts of pyrolysis temperature on lead adsorption by cotton stalk-derived biochar and related mechanisms. J. Environ. Chem. Eng. 9 (4), 105602.

Gunashova, G.Y., Ahmadova, F.R., Khalilov, R.I., 2021. Biosynthesis of silver nanoparticles using thermophilic *Bacillus* Sp. Б1 Advances in Biology & Earth Sciences 6 (2), 142–145.

Han, Y., Xu, H., Wang, G., Deng, P., Feng, L., Fan, Y., Zhang, J., 2023. Enhanced removal of estrogens from simulated wastewater by biochar supported nanoscale zero-valent iron: performance and mechanism. Biochar 5 (1).

Huang, Q., Cai, X., Chen, M., Yang, Q., Fan, S., Zhang, Y., Hu, H., Gan, T., Huang, Z., 2022. A stepwise processing strategy for treating manganese residue and the remediation of hexavalent chromium in water and soil by manganese residue-derived $(Fe,Mn)C_2O_4$. Chem. Eng. J. 436, 135258.

Javadian, H., Ruiz, M., Saleh, T.A., Sastre, A.M., 2020. Ca-alginate/carboxymethyl chitosan/$Ni_{0.2}Zn_{0.2}Fe_{2.6}O_4$ magnetic bionanocomposite: synthesis, characterization and application for single adsorption of Nd^{+3}, Tb^{+3}, and Dy^{+3} rare earth elements from aqueous media. J. Mol. Liq. 306, 112760.

Jia, X., Zhang, Y., He, Z., Chang, F., Zhang, H., Wågberg, T., Hu, G., 2021. Mesopore-rich badam-shell biochar for efficient adsorption of Cr(VI) from aqueous solution. J. Environ. Chem. Eng. 9 (4), 105634.

Khan, A.Z., Khan, S., Khan, M.A., Alam, M., Ayaz, T., 2020. Biochar reduced the uptake of toxic heavy metals and their associated health risk via rice (*Oryza sativa* L.) grown in Cr-Mn mine contaminated soils. Environ. Technol. Innov. 17, 100590.

Lawrinenko, M., Laird, D.A., Johnson, R.L., Jing, D., 2016. Accelerated aging of biochars: impact on anion exchange capacity. Carbon 103, 217–227.

Li, H., Zhao, Y., Xiao, Z., Yang, M., Zhou, B., 2021. Analysis on approximate site energy distribution and adsorption behaviors unveils reasons for highly efficient phosphorus removal by a novel sludge-based magnetic gel bead. Chem. Eng. J. 422, 130028.

Li, R., Wang, B., Wu, P., Zhang, J., Zhang, X., Chen, M., Cao, X., Feng, Q., 2023. Revealing the role of calcium alginate-biochar composite for simultaneous removing SO_4^{2-} and Fe^{3+} in AMD: adsorption mechanisms and application effects. Environ. Pollut. 329, 121702.

Lian, G., Wang, B., Lee, X., Li, L., Liu, T., Lyu, W., 2019. Enhanced removal of hexavalent chromium by engineered biochar composite fabricated from phosphogypsum and distillers grains. Sci. Total Environ. 697, 134119.

Liao, P., Li, B., Xie, L., Bai, X., Qiao, H., Li, Q., Yang, B., Liu, C., 2020. Immobilization of Cr(VI) on engineered silicate nanoparticles: microscopic mechanisms and site energy distribution. J. Hazard Mater. 383, 121145.

Liu, Y., Liu, H., Guo, S., Zhao, Y., Qi, J., Zhang, R., Ren, J., Cheng, H., Zong, M., Wu, X., Li, B., 2023. A review of carbon nanomaterials/bacterial cellulose composites for nanomedicine applications. Carbohydr. Polym. 323, 121445.

Luo, D., Geng, R., Zhang, Y., Li, P., Liang, J., Fan, Q., Qiang, S., 2022. Interaction behaviors of Cr(VI) at biotite-water interface in the presence of HA: batch, XRD and XPS investigations. Chemosphere 293, 133585.

Mousa, N.E., Simonescu, C.M., Pătescu, R.-E., Onose, C., Tardei, C., Culiță, D.C., Oprea, O., Patroi, D., Lavric, V., 2016. Pb^{2+} removal from aqueous synthetic solutions by calcium alginate and chitosan coated calcium alginate. React. Funct. Polym. 109, 137–150.

Nasibova, A., 2023. Generation of nanoparticles in biological systems and their application prospects. Adv. Biol. Earth Sci. 8 (2), 140–146.

Qian, L., Zhang, W., Yan, J., Han, L., Chen, Y., Ouyang, D., Chen, M., 2017. Nanoscale zero-valent iron supported by biochars produced at different temperatures: synthesis mechanism and effect on Cr(VI) removal. Environ. Pollut. 223, 153–160.

Qiu, Y., Zhang, Q., Gao, B., Li, M., Fan, Z., Sang, W., Hao, H., Wei, X., 2020. Removal mechanisms of Cr(VI) and Cr(III) by biochar supported nanosized zero-valent iron: synergy of adsorption, reduction and transformation. Environ. Pollut. 265, 115018.

Sahu, U.K., Ji, W., Liang, Y., Ma, H., Pu, S., 2022. Mechanism enhanced active biochar support magnetic nano zero-valent iron for efficient removal of Cr(VI) from simulated polluted water. J. Environ. Chem. Eng. 10 (2), 107077.

Seliem, M.K., Mobarak, M., Selim, A.Q., Mohamed, E.A., Halfaya, R.A., Gomaa, H.K., Anastopoulos, I., Giannakoudakis, D.A., Lima, E.C., Bonilla-Petriciolet, A., Dotto, G. L., 2020. A novel multifunctional adsorbent of pomegranate peel extract and activated anthracite for Mn(VII) and Cr(VI) uptake from solutions: experiments and theoretical treatment. J. Mol. Liq. 311, 113169.

Sun, S., Zeng, X., Gao, Y., Zhang, W., Zhou, L., Zeng, X., Liu, W., Jiang, Q., Jiang, C., Wang, S., 2021. Iron oxide loaded biochar/attapulgite composites derived camellia oleifera shells as a novel bio-adsorbent for highly efficient removal of Cr(VI). J. Clean. Prod. 317, 128412.

Teng, D., Zhang, B., Xu, G., Wang, B., Mao, K., Wang, J., Sun, J., Feng, X., Yang, Z., Zhang, H., 2020. Efficient removal of Cd(II) from aqueous solution by pinecone biochar: sorption performance and governing mechanisms. Environ. Pollut. 265, 115001.

Topaldemir, H., Tas, B., Yuksel, B., Ustaoglu, F., 2023. Potentially hazardous elements in sediments and *Ceratophyllum demersum*: an ecotoxicological risk assessment in Milic Wetland, Samsun, Turkiye. Environ. Sci. Pollut. Res. Int. 30 (10), 26397–26416.

Wan, Z., Cho, D.W., Tsang, D.C.W., Li, M., Sun, T., Verpoort, F., 2019. Concurrent adsorption and micro-electrolysis of Cr(VI) by nanoscale zerovalent iron/biochar/Ca-alginate composite. Environ. Pollut. 247, 410–420.

Wang, B., Gao, B., Fang, J., 2017a. Recent advances in engineered biochar productions and applications. Crit. Rev. Environ. Sci. Technol. 47 (22), 2158–2207.

Wang, B., Gao, B., Wan, Y., 2019a. Comparative study of calcium alginate, ball-milled biochar, and their composites on aqueous methylene blue adsorption. Environ. Sci. Pollut. Control Ser. 26 (12), 11535–11541.

Wang, B., Gao, B., Wan, Y., 2018a. Entrapment of ball-milled biochar in Ca-alginate beads for the removal of aqueous Cd(II). J. Ind. Eng. Chem. 61, 161–168.

Wang, B., Gao, B., Zimmerman, A.R., Lee, X., 2018b. Impregnation of multiwall carbon nanotubes in alginate beads dramatically enhances their adsorptive ability to aqueous methylene blue. Chem. Eng. Res. Des. 133, 235–242.

Wang, B., Gao, B., Zimmerman, A.R., Zheng, Y., Lyu, H., 2018c. Novel biochar-impregnated calcium alginate beads with improved water holding and nutrient retention properties. J. Environ. Manag. 209, 105–111.

Wang, B., Lian, G., Lee, X., Gao, B., Li, L., Liu, T., Zhang, X., Zheng, Y., 2019b. Phosphogypsum as a novel modifier for distillers grains biochar removal of phosphate from water. Chemosphere 238, 124684.

Wang, B., Wan, Y., Zheng, Y., Lee, X., Liu, T., Yu, Z., Huang, J., Ok, Y.S., Chen, J., Gao, B., 2019c. Alginate-based composites for environmental applications: a critical review. Crit. Rev. Environ. Sci. Technol. 49 (4), 318–356.

Wang, Q., Wang, B., Lee, X., Lehmann, J., Gao, B., 2018d. Sorption and desorption of Pb (II) to biochar as affected by oxidation and pH. Sci. Total Environ. 634, 188–194.

Wang, S., Gao, B., Li, Y., Creamer, A.E., He, F., 2017b. Adsorptive removal of arsenate from aqueous solutions by biochar supported zero-valent iron nanocomposite: batch and continuous flow tests. J. Hazard Mater. 322, 172–181.

Xu, H., Gao, M., Hu, X., Chen, Y., Li, Y., Xu, X., Zhang, R., Yang, X., Tang, C., Hu, X., 2021. A novel preparation of S-nZVI and its high efficient removal of Cr(VI) in aqueous solution. J. Hazard Mater. 416, 125924.

Yang, C., Ge, C., Li, X., Li, L., Wang, B., Lin, A., Yang, W., 2021a. Does soluble starch improve the removal of Cr(VI) by nZVI loaded on biochar? Ecotoxicol. Environ. Saf. 208, 111552.

Yang, S., Zhao, F., Sang, Q., Zhang, Y., Chang, L., Huang, D., Mu, B., 2021b. Investigation of 3-aminopropyltriethoxysilane modifying attapulgite for Congo red removal: mechanisms and site energy distribution. Powder Technol. 383, 74–83.

Yang, X., Zhou, T., Ren, B., Hursthouse, A., Zhang, Y., 2018. Removal of Mn (II) by sodium alginate/graphene oxide composite double-network hydrogel beads from aqueous solutions. Sci. Rep. 8 (1), 10717.

Yankovych, H., Novoseltseva, V., Kovalenko, O., Marcin Behunova, D., Kanuchova, M., Vaclavikova, M., Melnyk, I., 2021. New perception of Zn(II) and Mn(II) removal

mechanism on sustainable sunflower biochar from alkaline batteries contaminated water. J. Environ. Manag. 292, 112757.
Yi, Y., Wang, X., Ma, J., Ning, P., 2020. An efficient Egeria najas-derived biochar supported nZVI composite for Cr(VI) removal: characterization and mechanism investigation based on visual MINTEQ model. Environ. Res. 189, 109912.
Yüksel, B., Arıca, E., Söylemezoğlu, T., 2021a. Assessing reference levels of nickel and chromium in cord blood, maternal blood and placenta specimens from Ankara, Turkey. J. Turk. Ger. Gynecol. Assoc. 22 (3), 187–195.
Yüksel, B., Şen, N., Ögünç, G.I., Erdoğan, A., 2023. Elemental profiling of toxic and modern primers using ICP-MS, SEM-EDS, and XPS: an application in firearm discharge residue investigation. Aust. J. Forensic Sci. 55, 529–546.
Yüksel, B., Ustaoğlu, F., Arıca, E., 2021b. Impacts of a garbage disposal facility on the water quality of Çavuşlu Stream in Giresun, Turkey: a health risk assessment study by a validated ICP-MS assay. Aquat. Sci. Eng. 36 (4), 181–192.
Zhang, L., Dong, Y., Liu, J., Liu, C., Liu, W., Lin, H., 2022. The effect of co-pyrolysis temperature for iron-biochar composites on their adsorption behavior of antimonite and antimonate in aqueous solution. Bioresour. Technol. 347, 126362.
Zhang, X., Xu, H., Xi, M., Jiang, Z., 2023a. Removal/adsorption mechanisms of Cr(VI) and natural organic matter by nanoscale zero-valent iron-loaded biochar in their coexisting system. J. Environ. Chem. Eng. 11, 109860.
Zhang, Y., Jiao, X., Liu, N., Lv, J., Yang, Y., 2020. Enhanced removal of aqueous Cr(VI) by a green synthesized nanoscale zero-valent iron supported on oak wood biochar. Chemosphere 245, 125542.
Zhang, Z., Huang, G., Zhang, P., Shen, J., Wang, S., Li, Y., 2023b. Development of iron-based biochar for enhancing nitrate adsorption: effects of specific surface area, electrostatic force, and functional groups. Sci. Total Environ. 856 (Pt 1), 159037.
Zhao, C., Wang, B., Theng, B.K.G., Wu, P., Liu, F., Wang, S., Lee, X., Chen, M., Li, L., Zhang, X., 2021. Formation and mechanisms of nano-metal oxide-biochar composites for pollutants removal: a review. Sci. Total Environ. 767, 145305.
Zhao, F., Zhang, Y., Zheng, Z., Mu, B., 2022a. Synthesis of an absorption material based on oil shale semi-coke: discussion to adsorption mechanism and corresponding site energy distribution analysis. Colloids Surf. A Physicochem. Eng. Asp. 637, 128251.
Zhao, L., Zhao, Y., Nan, H., Yang, F., Qiu, H., Xu, X., Cao, X., 2020a. Suppressed formation of polycyclic aromatic hydrocarbons (PAHs) during pyrolytic production of Fe-enriched composite biochar. J. Hazard Mater. 382, 121033.
Zhao, M., Dai, Y., Zhang, M., Feng, C., Qin, B., Zhang, W., Zhao, N., Li, Y., Ni, Z., Xu, Z., Tsang, D.C.W., Qiu, R., 2020b. Mechanisms of Pb and/or Zn adsorption by different biochars: biochar characteristics, stability, and binding energies. Sci. Total Environ. 717, 136894.
Zhao, R., Wang, B., Wu, P., Feng, Q., Chen, M., Zhang, X., Wang, S., 2023a. Calcium alginate-nZVI-biochar for removal of Pb/Zn/Cd in water: insights into governing mechanisms and performance. Sci. Total Environ. 894, 164810.
Zhao, R., Wang, B., Zhang, X., Lee, X., Chen, M., Feng, Q., Chen, S., 2022b. Insights into Cr(VI) removal mechanism in water by facile one-step pyrolysis prepared coal gangue-biochar composite. Chemosphere 299, 134334.
Zhao, Z., Wang, B., Feng, Q., Chen, M., Zhang, X., Zhao, R., 2023b. Recovery of nitrogen and phosphorus in wastewater by red mud-modified biochar and its potential application. Sci. Total Environ. 860, 160289.
Zhao, Z., Wang, B., Zhang, X., Xu, H., Cheng, N., Feng, Q., Zhao, R., Gao, Y., Wei, M., 2022c. Release characteristics of phosphate from ball-milled biochar and its potential effects on plant growth. Sci. Total Environ. 821, 153256.
Zhou, H., Ye, M., Zhao, Y., Baig, S.A., Huang, N., Ma, M., 2022. Sodium citrate and biochar synergistic improvement of nanoscale zero-valent iron composite for the removal of chromium (VI) in aqueous solutions. J. Environ. Sci. 115, 227–239.
Zhuang, M., Wang, H., Qi, L., Cui, L., Quan, G., Yan, J., 2021. Production of activated biochar via a self-blowing strategy-supported sulfated nanoscale zerovalent iron with enhanced reactivity and stability for Cr(VI) reduction. J. Clean. Prod. 315, 128108.
Ziarati, P., Tajik, S., Sawicka, B., Cruz-Rodriguez, L., Vambol, V., Vambol, S., 2023. Detoxification of lead and cadmium in pharmaceutical effluent by home-made food wastes. Adv. Biol. Earth Sci. 8 (2), 129–139.